Supporting Information for

Effect of Electron-Nuclear Hyperfine Interactions on Multiple Quantum Coherences in Photogenerated Covalent Radical (Qubit) Pairs

Jordan N. Nelson, Jinyuan Zhang, Jiawang Zhou, Brandon K. Rugg, Matthew D. Krzyaniak, and Michael R. Wasielewski*

Department of Chemistry and Institute for Sustainability and Energy at Northwestern

Northwestern University, Evanston, Illinois 60208-3113

Contents

Synthesis and Characterization of TTF-ANI-PI_2

General Considerations. Reagents and solvents were purchased from commercial sources and used as received unless otherwise noted. Column chromatography was performed on standard silica gel, 60 angstrom, 32-63 μm (Sorbent Technologies). ^{1}H and ^{13}C NMR spectra were recorded on a Varian 500 MHz spectrometer at room temperature. ^{1}H and ^{13}C chemical shifts are listed in parts per million (ppm) and are referenced to residual protons or carbons of the deuterated solvents, respectively. High Resolution Mass Spectra (HRMS) were obtained with an Agilent LCTOF 6200 series mass spectrometer using electrospray ionization (ESI) and APPI.

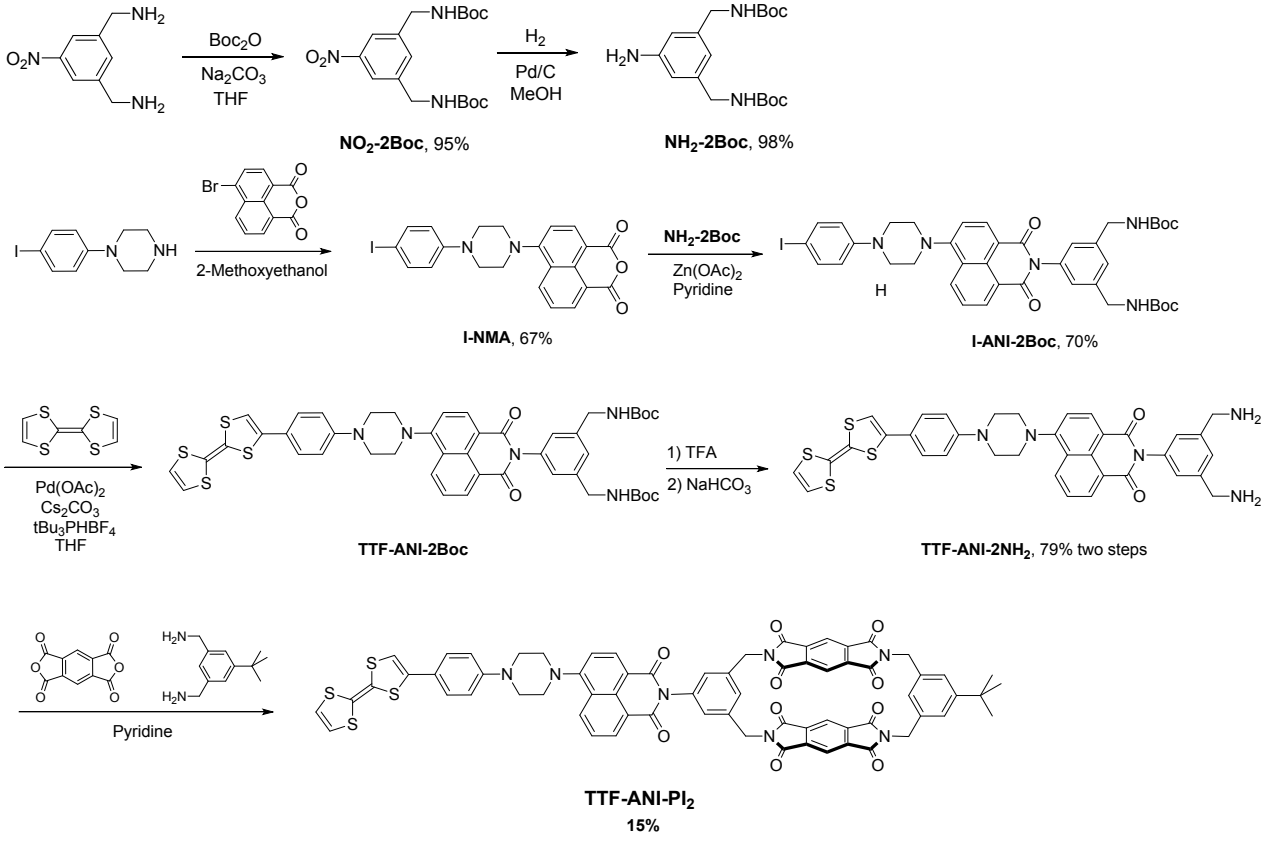

NO_2-2Boc. To a 50 mL round bottom flask 200 mg (1.1 mmol) **5-nitro-1,3-bis(diaminomethyl) benzene**,[1] 720 mg (3.3 mmol) Di-tert-butyl dicarbonate, and 700 mg Na_2CO_3 were added with 10 mL THF and 2 mL H_2O under nitrogen. The flask was then fit with a condenser and refluxed for 2 h. Upon reaction completion, the mixture was transferred to a separatory funnel, diluted with 20

mL DCM, and washed with saturated NaCl solution three times. The organic layer was collected, dried over Na_2SO_4, and the solvent removed under reduced pressure and produced 398 mg (95%) of **NO_2-2Boc**. The crude **NO_2-2Boc** was used for next step without further purification.

NH_2-2Boc. To a 25 mL 2-neck flask 390 mg (1.21 mmol) **NO_2-2Boc** and 20 mg 10% Pd/C were added with 10 mL MeOH. The flask was pump / purged with hydrogen three times and fit with a hydrogen balloon. The reaction was stirred at room temperature for 2 h and then filtered through Celite. The solvent was removed under reduced pressure to yield 352 mg (98%) of **NH_2-2Boc**. ^{1}H NMR (500 MHz, $CDCl_3$, δ): 6.52 (s, 1H), 6.47 (s 2H), 4.81 (s, 2H), 4.17 (s, 2H), 4.16 (s, 2H), 3.67 (s, 2H), 1.43 (s, 18H). ^{13}C NMR (100 MHz, $CDCl_3$, δ): 155.90, 147.05, 140.54, 116.54, 113.06, 79.45, 44.58, 28.44. ESI-HRMS (*m/z*): calculated for $C_{18}H_{29}N_3O_4Na$ $(M+Na)^+$: 374.2056, found: 374.2047 $(M+Na)^+$.

I-NMA. To a 10 mL round bottom flask 200 mg (0.7 mmol) 1-(4-iodophenyl)piperazine and 280 mg (1.0 mmol) 4-bromo-1,8-naphthalic anhydride were added with 5 mL 2-methoxyethanol. The reaction mixture was heated to reflux under nitrogen for 48 h. The solvent was then removed under reduced pressure. The residue solid was washed with ethyl acetate five times to give 227 mg (67%) of **1**. ^{1}H NMR (500 MHz, $CDCl_3$, δ): 8.60 (d, J = 6.5 Hz, 1H), 8.54 (d, J = 8.5 Hz, 1H), 8.49 (d, J = 6.5 Hz, 1H), 7.75 (t, J = 7.0 Hz, 1H), 7.57 (d, J = 9.0 Hz, 2H), 7.28 (d, J = 8.5 Hz, 1H), 6.77 (d, J = 9.0 Hz, 2H), 3.49-3.44 (m, 8H). ^{13}C NMR (125 MHz, $CDCl_3$, δ): 161.17, 160.48, 156.76, 150.53, 138.04, 134.87, 133.37, 132.28, 131.59, 126.24, 119.58, 118.46, 115.44, 111.52, 82.52, 52.78, 49.09. ESI-HRMS (*m/z*): calculated for $C_{22}H_{18}N_2O_3I$ $(M+H)^+$: 485.0362, found: 485.0347 $(M+H)^+$.

I-ANI-2Boc. To a 10 mL round bottom flask 150 mg (0.43 mmol) **NH_2-2Boc**, 210 mg (0.43 mmol) compound **I-NMA** and 100 mg (0.55 mmol) $Zn(OAc)_2 \cdot H_2O$ were added with 5 mL pyridine. The

reaction mixture was heated to reflux under nitrogen for 36 h. The solvent was then removed under reduced pressure. Purification via column chromatography (SiO_2, 25% ethyl acetate in $CHCl_3$) produced 244 mg (70%) of **2**. ^{1}H NMR (500 MHz, $CDCl_3$, δ): δ): 8.60 (d, *J* = 7.5 Hz, 1H), 8.54 (d, *J* = 8.5 Hz, 1H), 8.49 (d, *J* = 7.5 Hz, 1H), 7.73 (m, 1H), 7.57 (d, *J* = 8.5 Hz, 2H), 7.32 (s, 1H), 7.28 (d, *J* = 9.0 Hz, 1H), 7.12 (s, 2H), 6.78 (d, *J* = 9.0 Hz, 2H), 4.85 (br, 2H), 4.37 (s, 2H), 4.36 (s, 2H), 3.51-3.39 (m, 8H), 1.43 (s, 18H). ^{13}C NMR (125 MHz, $CDCl_3$, δ): 164.54, 164.05, 155.96, 155.81, 150.65, 140.68, 138.01, 136.16, 132.96, 131.65, 130.55, 130.27, 126.94, 126.37, 126.01, 123.37, 118.41, 117.07, 115.22, 82.32, 79.06, 52.92, 45.15, 44.42, 28.42. ESI-HRMS (*m/z*): calculated for $C_{40}H_{48}N_6O_6I$ $(M+NH_4)^+$: 835.2680, found: 835.2670 $(M+NH_4)^+$.

TTF-ANI-2Boc. To a 25 mL 2-neck flask 3 mg (0.01 mmol) *t*-Bu_3PHBF_4 70 mg (0.2 mmol) Cs_2CO_3 and 2 mg (0.01 mmol) $Pd(OAc)_2$ were added with 5 mL THF. The reaction mixture was heated to reflux under nitrogen for 30 min and allowed to cool to room temperature. Then 60 mg (0.073 mmol) **I-ANI-2Boc** and 45 mg (0.22 mmol) tetrathiafulvalene was added to the reaction vessel and heated to reflux for 48 h. Upon reaction completion, the mixture was transferred to a separatory funnel, diluted with DCM, and washed with saturated NaCl solution three times. The organic layer was collected, dried over Na_2SO_4, and the solvent removed under reduced pressure. The crude product was purified with silica gel plug (50% DCM in hexanes with 1% TEA) and yield 52 mg of **TTF-ANI-2Boc**. ^{1}H NMR (500 MHz, $CDCl_3$, δ): 8.63 (d, J = 7.5 Hz, 1H), 8.57 (d, J = 8.0 Hz, 1H), 8.51 (d, J = 8.0 Hz, 1H), 7.77-7.73. (m, 1H), 7.36 (d, *J* = 9.0 Hz, 2H), 7.33 (s, 1H), 7.30 (d, *J* = 8.0 Hz, 1H), 7.14 (s, 2H), 6.98 (d, *J* = 9.0 Hz, 2H), 6.37 (s, 1H), 6.33 (s, 2H), 4.87 (br, 2H), 4.39 (s, 2H), 4.38 (s, 2H), 3.55-3.45 (m, 8H), 1.45 (s, 18H). ^{13}C NMR (125 MHz, $CDCl_3$, δ):164.6, 164.1, 156.0, 155.8, 150.8, 140.7, 136.2, 135.9, 133.0, 131.7, 130.6, 130.3, 129.3, 127.4, 126.9, 126.4, 126.0, 124.4, 123.4, 119.1, 117.1, 116.4, 115.9, 115.2, 111.2, 110.8, 109.5,

79.6, 52.9, 48.6, 44.4, 28.4. ESI-HRMS (*m/z*): calculated for $C_{46}H_{47}N_5O_2S_4$ M^+: 893.2409, found: 893.2409 M^+.

TTF-ANI-2NH$_2$. To a 25 mL round bottom flask 52 mg of **TTF-ANI-2Boc** was added with 2 mL of DCM and then 1 mL of TFA was added dropwise. The mixture was stirred at room temperature for 30 minutes and slowly added 10 mL saturated $NaHCO_3$ solution. The resulting brown precipitate was filtered, washed with 50 mL water and 10 mL DCM. The product was dried under vacuum and yield 40 mg (79%, two-step) of the free base **TTF-ANI-2NH$_2$**. The crude **TTF-ANI-2NH$_2$** was used for next step without further purification.

TTF-ANI-PI$_2$. To a 250 mL oven dried round bottom flask, 46 mg (0.22 mmol) pyromellitic dianhydride was added with 60 mL of anhydrous pyridine. 20 mg (0.1 mmol) **5-*t*-butyl-1,3-bis(diaminomethyl)benzene**[2] and 70 mg (0.1 mmol) compound **3** were dissolved in 60 mL of anhydrous pyridine and slowly added to the flask simultaneously. The flask was then fitted with a condenser and heated to reflux for 12 h under nitrogen. The solvent was removed under reduced pressure. Purification via preparative thin-layer and column chromatography (alumina N, 10% acetone in DCM) produced 19 mg (15%) of **TTF-ANI-PI$_2$**. ^{1}H NMR (500 MHz, $CDCl_3$, δ): 8.55 (d, J = 7.5 Hz, 1H), 8.50 (d, J = 8.0 Hz, 2H), 8.21 (d, *J* = 8.0 Hz, 1H), 8.11 (s, 4H), 7.74-7.71 (m, *2*H), 7.39-7.44 (m, 2H), 7.34 (d, J = 1.5 Hz, 2H), 7.31 (d, J = 1.5 Hz, 2H), 7.27 (d, J = 8 Hz, 2H), 6.96 (d, J = 8 Hz, 2H), 6.35 (s, 1H), 6.32 (s, 2H), 4.86 (s, 4H), 4.82 (s, 4H), 3.55-3.41 (m, 8H), 1.27 (s, 9H). ^{13}C NMR (125 MHz, $CDCl_3$, δ): 164.8, 164.6, 164.3, 164.1, 163.2, 162.7, 154.9, 151.2, 137.1, 136.3, 166.2, 135.9, 134.8, 132.8, 132.0, 130.7, 129.5, 129.2, 129.0, 128.9, 128.7, 126.4, 126.3, 125.3, 125.2, 125.1, 124.9, 122.2, 118.1, 117.1, 115.9, 114.8, 114.1, 51.9, 47.9, 41.1, 40.5, 33.7, 30.9, 30.2, 28.7. ESI-HRMS (*m/z*): calculated for $C_{68}H_{48}N_7O_{10}S_4$ $(M+H)^+$: 1250.2345, found: 1250.2290 $(M+H)^+$.

Difference in Gaussian Distributions of Electron-Nuclear Hyperfine Interactions

To arrive at ΔE_{HFI}, consider that electron 1 of an SCRP with electron spin moment S in the direction of the magnetic field randomly experiences an ensemble average of a large number of nuclear spin configurations with nuclear spin moment I; so, according to the Central Limit Theorem, this interaction will approach a Gaussian probability distribution.[3,4]

$$\lim_{j\to\infty}\sum_j \alpha_{1j} I_j = \lim_{j\to\infty} A_1 = N(A_1,\sigma_1) = \frac{1}{\sqrt{2\pi{\sigma_1}^2}}\exp\left(-\frac{(A-A_1)^2}{2{\sigma_1}^2}\right) \quad \text{(S1)}$$

where A_1 is defined above as the sum total isotropic electron-nuclear hyperfine interaction for electron 1 and σ_1 is its root-mean squared standard deviation:[5]

$$\sigma_{1j} = \left[\sum_j {\alpha_{1j}}^2 I_j(I_j+1)\right]^{1/2} \quad \text{(S2)}$$

Because the vector S_z of each spin in the direction of the magnetic field is opposite for $|S\rangle$ and $|T_0\rangle$, the resulting distribution is a difference between these Gaussian distributions—itself a Gaussian:

$$\Delta_{ST_0} N_{HFI,}(A) = N(A_1,\sigma_1) - N(A_2,\sigma_2) = \frac{\exp\{-[A-(A_1-A_2)]^2/[2({\sigma_1}^2+{\sigma_2}^2)]\}}{\sqrt{\{2\pi({\sigma_1}^2+{\sigma_2}^2)\}}} \quad \text{(S3)}$$

Due to the localized nature of each electron in the spin-correlated RP and the molecular length scale considered in this work (ca. 30 Å), this description specifically assumes that a given nucleus j interacts only with one electron or the other – that is the interaction between nucleus j and the other electron in the RP is negligible. In other cases, A_1 and σ_{1j} could be generalized to include a sum over all of the electrons interacting with nucleus j. As described in the main text, one can arrive at ΔE_{HFI}, the contribution of ΔN_{HFI} to the line-broadening of the forbidden quantum beats, by taking the sum of the Gaussian integral of $N(A_1,\sigma_1)$ and $N(A_2,\sigma_2)$ individually, weighted by the numerical average between the two.

Density Matrix Formalism for Multiple-Quantum Coherences in Spin-correlated RPs

Given the high magnetic field typically (>>kT) used in EPR experiments like those presented here (ca. 340 mT), only the mixed states $|\Phi_A\rangle$ or $|\Phi_B\rangle$ defined in the main text (Figure 1A) are initially populated and double-quantum ($\Delta m_s = \pm 2$) coherences (DQC) between unpopulated $|T_+\rangle$ and $|T_-\rangle$ would seem insignificant. However, because a spin-correlated RP is actually a fundamental example of an entangled 2-qubit system, the four spin states and the transitions between them are more completely described by a discretely-quantized, 4x4 density matrix. In this representation, populations are described on the diagonal of the density matrix, and coherences are on the off-diagonal (Figure 1B). This density matrix can be arrived at by first taking the spin Hamiltonian, and applying it to either the default ($|S\rangle$, $|T_0\rangle$, $|T_+\rangle$, $|T_-\rangle$) or mixed ($|\Phi_A\rangle$, $|\Phi_B\rangle$, $|T_+\rangle$, $|T_-\rangle$) basis. With $\hbar \equiv 1$, the spin Hamiltonian chosen takes the form:

$$H = S_{1z}(g_1\mu_B B_0 - \Omega) + S_{2z}(g_2\mu_B B_0 - \Omega) + S_{1z}N(A_1,\sigma_1) + S_{2z}N(A_2,\sigma_2)$$
$$+J\left(\frac{1}{2} - 2S_1 \cdot S_2\right) + \frac{1}{2}D(3\cos^2\zeta - 1)[{S_z}^2 - \frac{1}{3}S(S+1)] \qquad \text{(S3)}$$

Where S_{1z}, S_{2z} are the respective radical spins in the direction of the constant magnetic field B_0, Ω is the static μw frequency, $g_1$and g_2 are the g-factors of the radicals spin S_1 and S_2, μ_B is the Bohr magneton, $N(A_1,\sigma_1)$ and $N(A_2,\sigma_2)$ are defined in eq. S1, J and D are the electron-electron exchange and dipolar interaction, respectively, ζ is the angle between the principal axis of dipolar interaction and external magnetic field, and S and I are the usual spin operators. This spin Hamiltonian is identical to that used by Tang and Norris[6-7] except with the Gaussian ensemble interpretation of the hyperfine interaction $N(A_1,\sigma_1)$ substituted. The theoretical description of multi-quantum coherences in spin-correlated RPs that we use here was originally developed by Tang and Norris,[8-10] but we have included the density matrix formalism here for the reader's benefit and for consistency in notation.

To begin with, in the organic molecules in this work, the initial density matrix is pure singlet and the 7 ns laser pulse is short enough to be considered instantaneous on the EPR timescale, such that $\sigma(0)$ is pure singlet. That is,

$$\sigma(0) = \begin{bmatrix} \langle T_+ | T_+ \rangle & 0 & 0 & 0 \\ 0 & \langle S | S \rangle & 0 & 0 \\ 0 & 0 & \langle T_0 | T_0 \rangle & 0 \\ 0 & 0 & 0 & \langle T_+ | T_+ \rangle \end{bmatrix} = \begin{bmatrix} 0 & 0 & 0 & 0 \\ 0 & 1 & 0 & 0 \\ 0 & 0 & 0 & 0 \\ 0 & 0 & 0 & 0 \end{bmatrix}$$

(S10)

With minimal spin-orbit coupled organic radical pairs, then, one of the five key elements of DiVincenzo's criteria for a universal quantum computing is met: the ability to initialize the state of the spin qubits to a simple fiducial state.[11]

Second, after photoexcitation and electron transfer relevant to the molecules in the main text, with an arbitrary orientation ζ for D and in the mixed-state basis (for convenience in presenting the eigenvalues), the eigenvalues are:

$$E_1 = \langle T_+ | H | T_+ \rangle = \frac{1}{2}\left[B_0\mu_B(g_1 + g_2) - 2\Omega + N(A_1,\sigma_1) + N(A_2,\sigma_2) + \frac{1}{3}D(3\cos^2\zeta - 1)\right] \quad \text{(S4)}$$

$$E_2 = \langle \Phi_A | H | \Phi_A \rangle = J - \frac{1}{6}D(3\cos^2\zeta - 1) + \frac{1}{2}E_{23} \quad \text{(S5)}$$

$$E_3 = \langle \Phi_B | H | \Phi_B \rangle = J - \frac{1}{6}D(3\cos^2\zeta - 1) - \frac{1}{2}E_{23} \quad \text{(S6)}$$

$$E_4 = \langle T_- | H | T_- \rangle = -E_1$$

(S7)

Where

$$E_{23} = E_2 - E_3 = \sqrt{\left[J - \frac{1}{6}D(3\cos^2\zeta - 1)\right]^2 + \frac{1}{4}[B_0\mu_B(g_1 - g_2) + \Delta_{ST_0}N_{HFI}]} \quad \text{(S8)}$$

Third, returning to the default basis ($|S\rangle$, $|T_0\rangle$, $|T_+\rangle$, $|T_-\rangle$), after a time T_{DAF} following the laser pulse, the density matrix σ evolves as:

$$\sigma(T_{\mathrm{DAF}}) = e^{-iHt}\sigma(0)e^{iHt} = \begin{bmatrix} 0 & 0 & 0 & 0 \\ 0 & 1-G & F & 0 \\ 0 & F^{\ddagger} & G & 0 \\ 0 & 0 & 0 & 0 \end{bmatrix},$$

Where, with ϕ defined in eq. 4 in the main text,

$$G(T_{\mathrm{DAF}}) = \frac{1}{2}\sin^2 2\phi(1-\cos E_{23}T_{\mathrm{DAF}}),$$

$$F(T_{\mathrm{DAF}}) = \frac{1}{2}\sin 2\phi(1-\cos E_{23}T_{\mathrm{DAF}}) \qquad \text{(S9)}$$

The matrix element F (and $F^{\ddagger}$) corresponds to ZQC and are fed by the $|S\rangle$ and $|T_0\rangle$ populations, all of which oscillate in time according to the energy difference E_{23} and with a coefficient defined by ϕ. From the expressions in eq S9, one can clearly see again the importance of ϕ in forbidden coherences, which is governed by the ratio of $g_1 - g_2$ and $\Delta_{ST_0}N_{HFI}$ vs J and D (main text eq. 4).

Fourth, the density matrix at the time of the first $\frac{\pi}{2}$ microwave pulse with an arbitrary phase angle ξ off of the *x*-axis of the EPR spectrometer is given by

$$\sigma_{\frac{\pi}{2},\xi}(T_{\mathrm{DAF}}) = \exp\left[-\frac{1}{2}\pi\mathrm{i}(S_x\cos\xi + S_y\sin\xi)\right]\sigma(T_{\mathrm{DAF}})\exp\left[\frac{1}{2}\pi\mathrm{i}(S_x\cos\xi + S_y\sin\xi\right) =$$
$$\begin{bmatrix} \frac{1}{2}G(T_{\mathrm{DAF}}) & -\frac{\mathrm{i}}{\sqrt{2}}F^{\ddagger}(T_{\mathrm{DAF}})e^{-\mathrm{i}\xi} & 0 & \frac{1}{2}G(T_{\mathrm{DAF}})e^{-\mathrm{i}2\xi} \\ 0 & 1-G(T_{\mathrm{DAF}}) & 0 & 0 \\ 0 & 0 & G & 0 \\ \frac{1}{2}G(T_{\mathrm{DAF}})e^{-\mathrm{i}2\xi} & -\frac{\mathrm{i}}{\sqrt{2}}F^{\ddagger}(T_{\mathrm{DAF}})e^{\mathrm{i}\xi} & 0 & \frac{1}{2}G(T_{\mathrm{DAF}}) \end{bmatrix} \qquad \text{(S11)}$$

Single- and double-quantum coherences correspond to the matrix elements in eq. S11 with phase factors of ξ and 2ξ. From eq. S11, one can also see that no zero-quantum coherence (ZQC) is generated from the first microwave pulse; rather, it is entirely dependent on state mixing, which, in this case, is initiated by the laser pulse (eq. S9).

Fourth, the density matrix after time τ is given by

$$\sigma_{\frac{\pi}{2},\xi}(T_{\mathrm{DAF}},\tau) = \exp(-\mathrm{i}H\tau)\sigma_{\frac{\pi}{2},\xi}(T_{\mathrm{DAF}})\exp(\mathrm{i}H\tau)$$

As the matrix elements become somewhat large to write out, with reference to the elements of eq S11 bracketed, they can be considered element-by-element as:

$$\sigma_{\frac{\pi}{2},\xi}(T_{\mathrm{DAF}},\tau)_{11} = \sigma_{\frac{\pi}{2},\xi}(T_{\mathrm{DAF}})_{11}$$

$$\sigma_{\frac{\pi}{2},\xi}(T_{\mathrm{DAF}},\tau)_{12} = [\sigma_{\frac{\pi}{2},\xi}(T_{\mathrm{DAF}})_{12}](\cos^2\phi e^{-\mathrm{i}E_{12}\tau} + \sin^2\phi e^{-\mathrm{i}E_{13}\tau})$$

$$\sigma_{\frac{\pi}{2},\xi}(T_{\mathrm{DAF}},\tau)_{13} = \frac{1}{2}[\sigma_{\frac{\pi}{2},\xi}(T_{\mathrm{DAF}})_{12}]\sin 2\phi(e^{-\mathrm{i}E_{12}\tau} + e^{-\mathrm{i}E_{13}\tau})$$

$$\sigma_{\frac{\pi}{2},\xi}(T_{\mathrm{DAF}},\tau)_{14} = \frac{1}{2}G(T_{\mathrm{DAF}})e^{-\mathrm{i}2\xi}e^{-\mathrm{i}E_{14}\tau}$$

$$\sigma_{\frac{\pi}{2},\xi}(T_{\mathrm{DAF}},\tau)_{22} = [\sigma_{\frac{\pi}{2},\xi}(T_{\mathrm{DAF}})_{22}]\{1 - \frac{1}{2}\sin^2 2\phi(1 - \cos E_{23}\tau)\}$$

$$\sigma_{\frac{\pi}{2},\xi}(T_{\mathrm{DAF}},\tau)_{23} = \frac{1}{2}[\sigma_{\frac{\pi}{2},\xi}(T_{\mathrm{DAF}})_{22}]\{\sin 2\phi(\cos 2\phi(1 - \cos E_{23}\tau) + \mathrm{i}\sin E_{23}\tau\}$$

$$\sigma_{\frac{\pi}{2},\xi}(T_{\mathrm{DAF}},\tau)_{24} = [\sigma_{\frac{\pi}{2},\xi}(T_{\mathrm{DAF}})_{24}](\cos^2\phi e^{-\mathrm{i}E_{24}\tau} + \sin^2\phi e^{-\mathrm{i}E_{34}\tau})$$

$$\sigma_{\frac{\pi}{2},\xi}(T_{\mathrm{DAF}},\tau)_{33} = \frac{1}{2}[\sigma_{\frac{\pi}{2},\xi}(T_{\mathrm{DAF}})_{22}]\sin^2 2\phi(1 - \cos E_{23}\tau)$$

$$\sigma_{\frac{\pi}{2},\xi}(T_{\mathrm{DAF}},\tau)_{34} = \frac{1}{2}[\sigma_{\frac{\pi}{2},\xi}(T_{\mathrm{DAF}})_{24}]\sin 2\phi(e^{-\mathrm{i}E_{24}\tau} + e^{-\mathrm{i}E_{34}\tau})$$

$$\sigma_{\frac{\pi}{2},\xi}(T_{\mathrm{DAF}},\tau)_{34} = \sigma_{\frac{\pi}{2},\xi}(T_{\mathrm{DAF}})_{11}$$

And for the remaining conjugate matrix elements:

$$\sigma_{\frac{\pi}{2},\xi}(T_{\mathrm{DAF}},\tau)_{mn} = \sigma_{\frac{\pi}{2},\xi}{}^{\ddagger}(T_{\mathrm{DAF}},\tau)_{nm} \qquad \text{(S12)}$$

The elements in eq. S12 therefore also demonstrate a dependence on τ, the time between the microwave pulses. Additionally, one can see that the elements like $\sigma_{\frac{\pi}{2},\xi}(T_{\mathrm{DAF}},\tau)_{22}$ corresponding

to ZQC are indeed nonzero and beat with frequency related to E_{23}. Moreover, the double-quantum coherences (phase 2ξ) in eq. S12 are still not present in the SQC matrix elements (nm=1,2; 1,3; 2,3; 3,4 and their conjugates) corresponding to observable transverse magnetization.

Therefore, for detection of DQC, another $\frac{\pi}{2}$ microwave pulse is necessary to transfer the coherence to the transverse magnetization elements (nm=1,2; 1,3; 2,3; 3,4 and their conjugates). In quadrature detection, the corresponding observables as a function of t after the second microwave pulse are the trace of the S_x and S_x spin operators, respectively, with the corresponding matrix elements such that:

$$\langle S_x(T_{\mathrm{DAF}},\tau,t)\rangle_{2Q} = \frac{1}{4}\sin^2 2\phi(1-\cos E_{23}T_{\mathrm{DAF}})\sin(E_{14}\tau+2\xi)\times[\sin^2 2\phi(\cos E_{23}t-\cos E_{23}t)+\cos^2 2\phi(\cos E_{13}t-\cos E_{34}t)$$

$$\langle S_x(T_{\mathrm{DAF}},\tau,t)\rangle_{1Q} = \frac{1}{4\sqrt{2}}\left[\sin 2\phi\left(e^{-\mathrm{i}E_{12}t}-e^{-\mathrm{i}E_{13}t}-e^{-\mathrm{i}E_{24}t}+e^{-\mathrm{i}E_{34}t}\right)\right]\left[\sigma_{\frac{\pi}{2},\xi}(T_{\mathrm{DAF}},\tau)_{12}-\sigma^{\ddagger}_{\frac{\pi}{2},\xi}(T_{\mathrm{DAF}},\tau)_{24}\right]+\frac{1}{2\sqrt{2}}\left[\sin^2\phi\left(e^{\mathrm{i}E_{12}t}+e^{-\mathrm{i}E_{24}t}\right)+\cos^2\phi\left(e^{\mathrm{i}E_{13}t}+e^{-\mathrm{i}E_{34}t}\right)\right]\left[\sigma_{\frac{\pi}{2},\xi}(T_{\mathrm{DAF}},\tau)_{13}+\sigma^{\ddagger}_{\frac{\pi}{2},\xi}(T_{\mathrm{DAF}},\tau)_{34}\right]+herm.conj.$$

$$\langle S_x(T_{\mathrm{DAF}},\tau,t)\rangle_{0Q} = \frac{1}{4}\sin^2 2\phi\left[1-\frac{1}{2}\sin^2 2\phi(1-\cos E_{23}T_{\mathrm{DAF}})\right]\{\cos 2\phi(1-\cos E_{23}\tau)\times[\sin E_{12}t-\sin E_{24}t-\sin E_{13}t+\sin E_{34}t]+\sin E_{23}\tau[\sin E_{12}T+\cos E_{24}t-\cos E_{13}t-\cos E_{34}t]\}$$

$$\langle S_y(T_{\mathrm{DAF}},\tau,t)\rangle_{2Q} = \frac{1}{4}\sin^2 2\phi(1-\cos E_{23}T_{\mathrm{DAF}})\cos(E_{14}\tau+2\xi)\times[\sin^2\phi(\cos E_{12}t-\cos E_{24}t)+\cos^2\phi(\cos E_{13}t+\cos E_{34}t)$$

$$\langle S_y(T_{\mathrm{DAF}},\tau,t)\rangle_{1Q}$$
$$= \frac{\mathrm{i}}{4\sqrt{2}}\left[\sin 2\phi\left(e^{-\mathrm{i}E_{12}t} - e^{-\mathrm{i}E_{13}t} + e^{\mathrm{i}E_{24}t} - e^{\mathrm{i}E_{34}t}\right)\right]\left[\sigma_{\frac{\pi}{2},\xi}(T_{\mathrm{DAF}},\tau)_{12} + \sigma^{\ddagger}_{\frac{\pi}{2},\xi}(T_{\mathrm{DAF}},\tau)_{24}\right]$$
$$+ \frac{\mathrm{i}}{2\sqrt{2}}\left[\sin^2\phi\left(e^{\mathrm{i}E_{12}t} + e^{-\mathrm{i}E_{24}t}\right) + \cos^2\phi\left(e^{\mathrm{i}E_{13}t} - e^{-\mathrm{i}E_{34}t}\right)\right]\left[\sigma_{\frac{\pi}{2},\xi}(T_{\mathrm{DAF}},\tau)_{13} - \sigma^{\ddagger}_{\frac{\pi}{2},\xi}(T_{\mathrm{DAF}},\tau)_{34}\right] + herm.conj.$$

$$\langle S_x(T_{\mathrm{DAF}},\tau,t)\rangle_{0Q} = \frac{1}{4}\sin^2 2\phi\left[1 - \frac{1}{2}\sin^2 2\phi(1-\cos E_{23}T_{\mathrm{DAF}})\right]\{\cos 2\phi(1-\cos E_{23}\tau)$$
$$\times\left[\cos E_{12}t - \cos E_{24}t - \cos E_{13}t + \cos E_{34}t\right] - \sin E_{23}\tau\left[\sin E_{12}T + \sin E_{24}t - \sin E_{13}t - \sin E_{34}t\right]\}$$

Although there is no population difference between $|T_+\rangle$ or $|T_-\rangle$ in the four-level energy diagram interpretation of a spin-correlated radical pairs, at last one can see from the above derivation how double-quantum coherence can still be measured in pulsed-EPR and measured with a simple laser-T_{DAF}-$\frac{\pi}{2}$μw pulse-τ-$\frac{\pi}{2}$μw pulse-t pulse sequence.

Also of importance, from these final expressions, it is clear how the phase offset in the double- and single- (embedded in the $\sigma_{\frac{\pi}{2},\xi}$ elements) can be used, as in the experimental results in this work. By cycling the phase ξ relative to the other pulse between 0, $\pi/2$, π, and $3\pi/2$, and collecting simultaneously $\langle S_x \rangle$ and $\langle S_y \rangle$ in quadrature, one can then process the same set of phase-cycled signals with a weighting factor $e^{-im\xi}$ for each m-order quantum coherence (Table S1). In this way, a consistent set of data in phase space can be used to phase cycle multidimensional time-domain pulsed EPR experiments. This provides the most experimentally consistent method to compare quantum-ordered coherences as they appear in the density matrix for quantum tomography—or to focus specifically on the fastest-relaxing quantum-ordered coherences as is done in this work.

Table S1. Selective 4-step phase cycles used to obtain the zero-, single-, and double quantum coherences in the pulse-EPR measurements on **TTF$^{\bullet+}$-ANI-PI$^{\bullet-}$** and **TTF$^{\bullet+}$-ANI-PI$_2^{\bullet-}$**.

Step →	1		2		3		4	
	P_1	P_2	P_1	P_2	P_1	P_2	P_1	P_2
ZQC	+x	+x	+y	+x	-x	+x	-y	+x
SQC	+x	+x	-x	+y	+x	-x	-x	-y
DQC	+x	+x	-y	-x	-x	+x	-x	-y

Transient Optical Absorption Spectroscopy

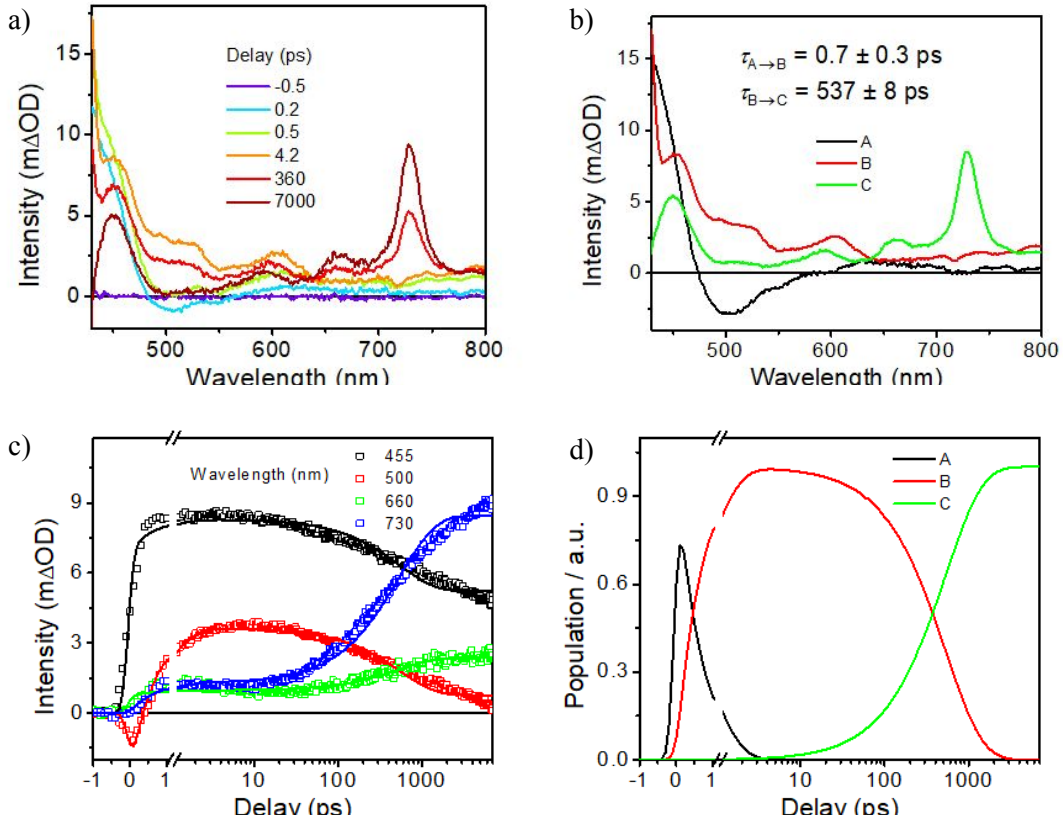

Figure S1. (a) Femtosecond TA spectrum of **TTF-ANI-PI** in PrCN at 105K; (b) species-associated spectra after photoexcitation; (c) the global fit of the species in (b) to specific wavelengths in the spectra of (a); and (d) the relative population kinetics of the of the species in (b).

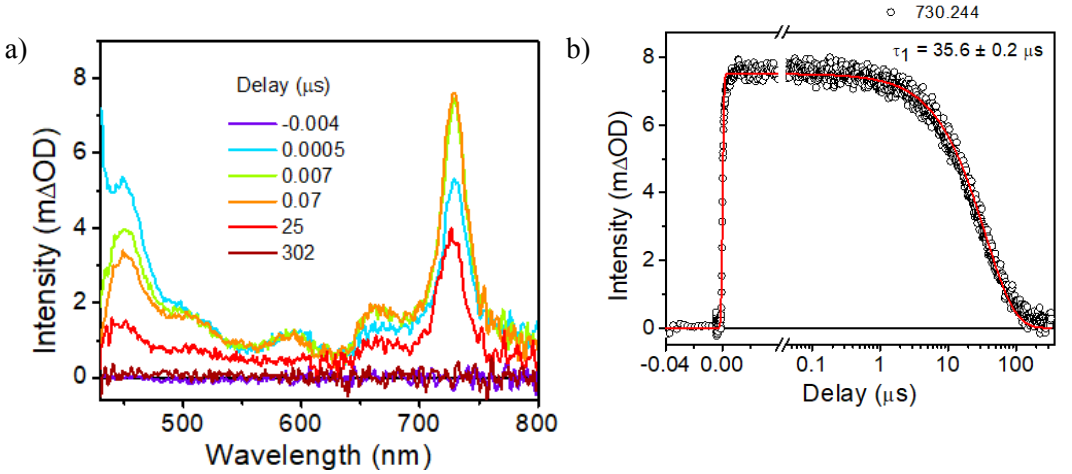

Figure S2. (a) Nanosecond TA spectrum of **TTF-ANI-PI** in PrCN at 105K; (b) Single-wavelength (730 nm) fit to the spectrum in (a). The average kinetic lifetime weighted by the relative proportion of each kinetic component is presented in bold and is used as measure of the charge recombination time constant of **PI**$^{\bullet}$ to ground state in Figure 2 in the main text.

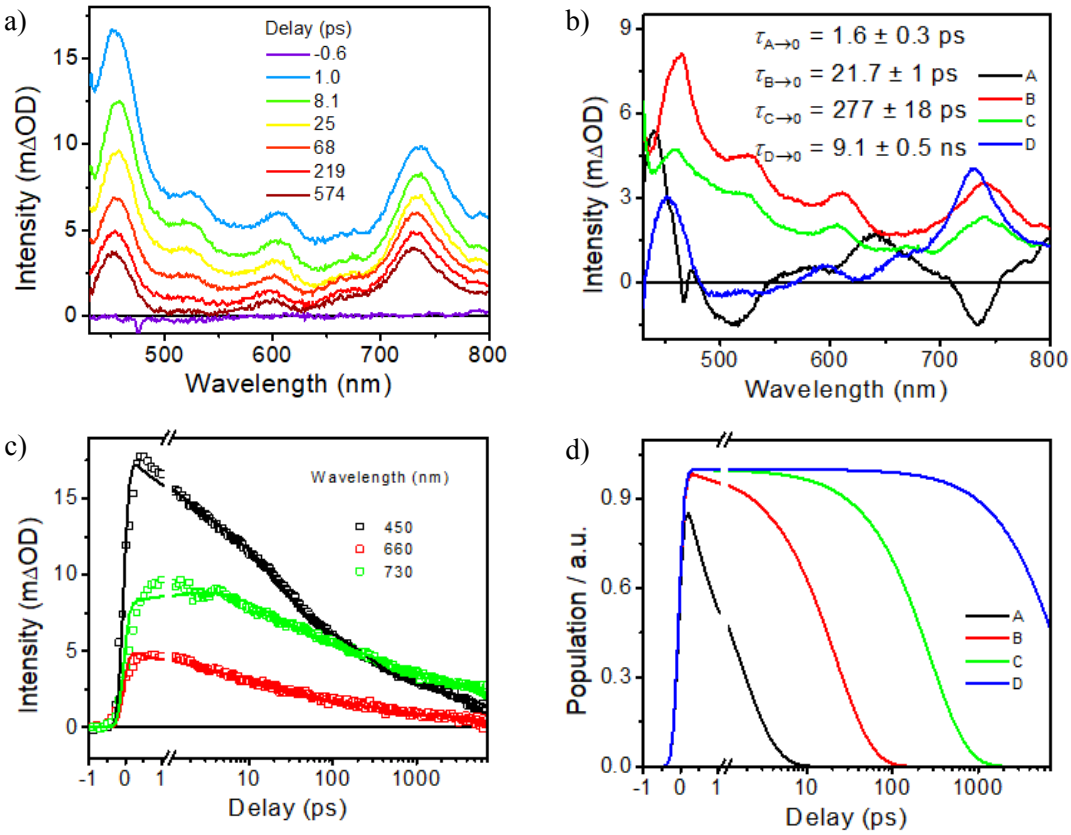

Figure S3. (a) Femtosecond TA spectrum of **TTF-ANI-PI$_2$** in PrCN at 105K; (b) species-associated spectra after photoexcitation; (c) the global fit of components in (b) to specific wavelengths in the spectra of (a); and (d) the relative population kinetics of the components in (b).

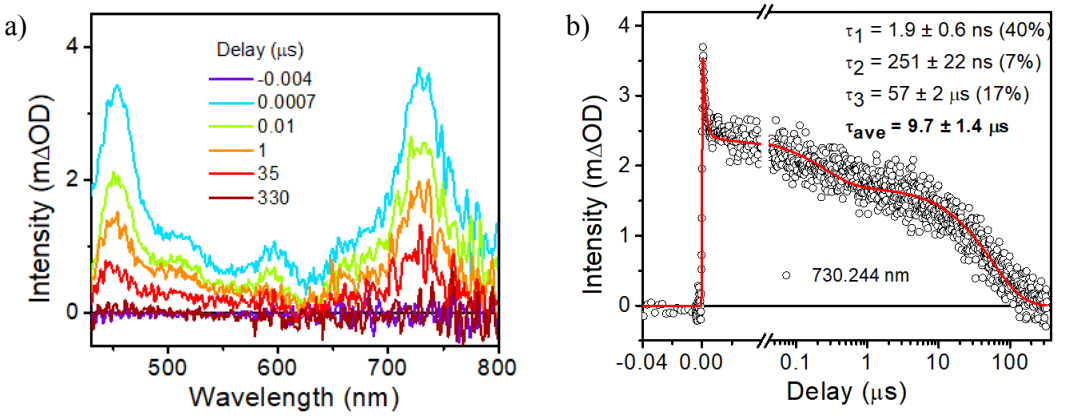

Figure S4. (a) Nanosecond TA spectrum of **TTF-ANI-PI$_2$** in PrCN at 105K; (b) Single-wavelength (730 nm) fit to the spectrum in (a). The average kinetic lifetime weighted by the relative proportion of each kinetic component is presented in bold and is used as measure of the charge recombination of **PI$_2^{-\bullet}$** to ground state in Figure 2 in the main text.

CW-ENDOR Spectroscopy

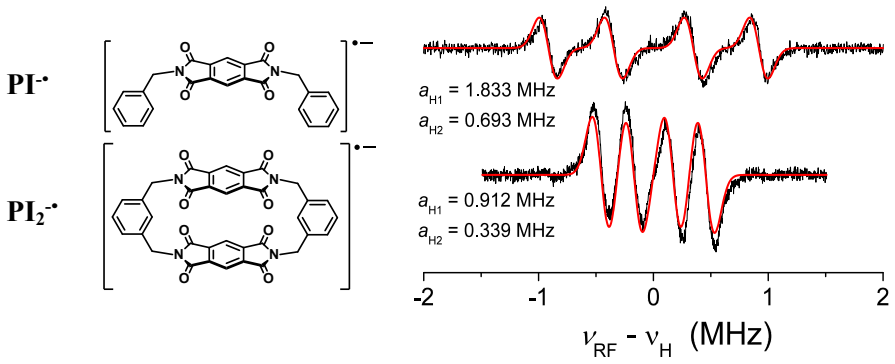

Figure S5. CW-ENDOR spectra of the chemically generated radicals **PI**$^{-\bullet}$ (top) and **PI**$_2^{-\bullet}$ (bottom) at (270K in CH_3CN); the black trace is experimental data, and the red is a fit using the inset proton hyperfine parameters.

Two-dimensional Time-domain EPR spectroscopy

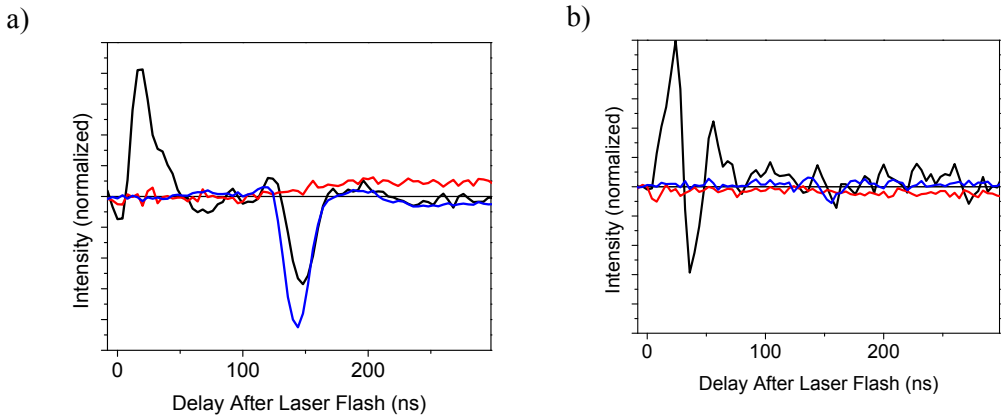

Figure S6. Real signal channel of quantum beats as delay after the 416 nm laser flash is incremented for (a) **TTF**$^{+\bullet}$**-ANI-PI**$^{-\bullet}$ and (b) **TTF**$^{+\bullet}$**-ANI-PI**$_2^{-\bullet}$. The black, red, and blue traces use the zero-, single-, and double quantum coherence phase cycle (Table 1, main text), respectively. The integration limits are the same as those used in Figure 4.

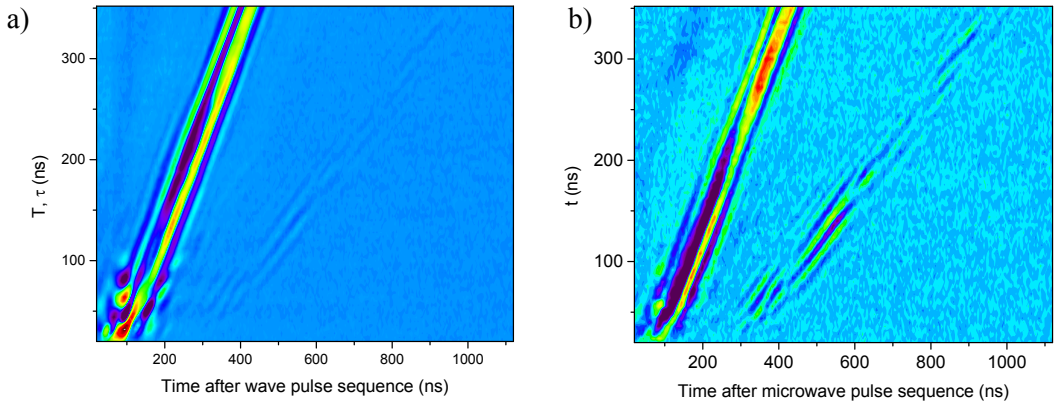

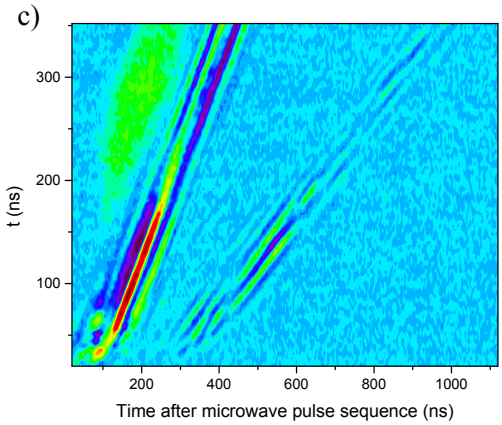

Figure S7. (a) Real channel of complex signal with no phase cycle collected simultaneously with imaginary channel from Figure 5 in the main text; Imaginary channel (b) and real channel (c) from complex signal with double-quantum phase cycle showing enhancement of the double quantum coherence.

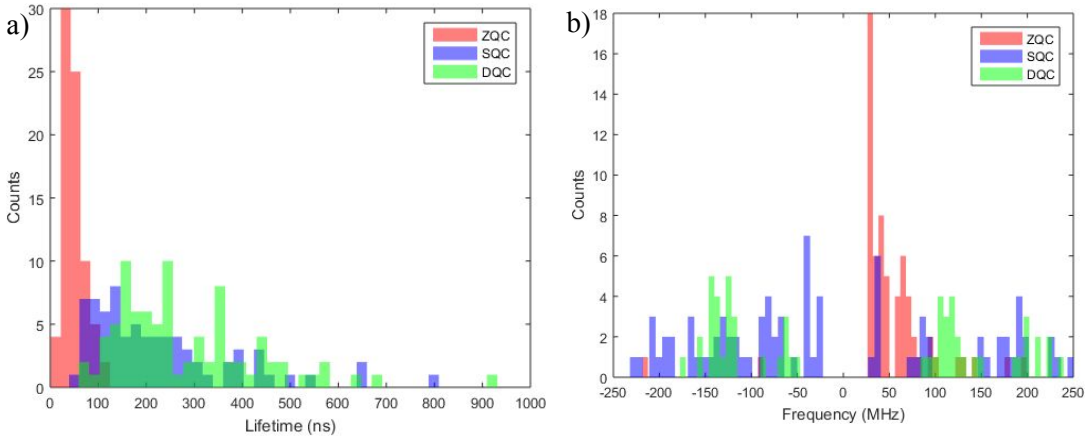

Figure S8. Distribution (a) of the inverse of damping coefficients ('lifetime') and distribution of frequencies (b) from LPSVD of the phase cycles (ZQC,SQC, DQC, respectively) specific to each of the coherences. Note that although the lifetimes for SQC and DQC phase-sensitized spectra are rational (lifetime(DQC or SQC) > lifetime(ZQC)), the kurtosis of DQC and SQC frequencies indicate the need for a longer-time experiment or greater averaging to approach with confidence the line broadening analysis presented in Figure 6.

OOP-ESEEM of TTF-ANI-PI and TTF-ANI-PI$_2$ at 85K

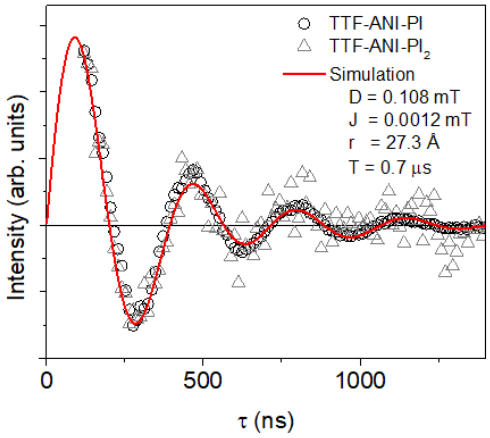

Figure S9. Out-of-phase electron-envelope modulation (OOP-ESEEM) of **TTF-ANI-PI** (circles) and **TTF-ANI-PI$_2$** (triangles) in toluene-d_8 at 85K. A simulation is provided in red with fit parameters inset (J and D are the electron-electron exchange and dipolar coupling, respectively; r is the RP distance in a point-dipole approximation; T is the lifetime or relaxation constant of the RP.

We have performed out-of-phase electron-envelope modulation (OOP-ESEEM) experiments on **TTF-ANI-PI** previously,[12] but not for **TTF-ANI-PI$_2$** has not, which is now provided in Figure S2. The integration bounds and pulse sequences are the same as that utilized earlier.[12] A simulation was performed with all values in the spin Hamiltonian fixed using the J, D and r determined earlier for **TTF-ANI-PI** with the relaxation time constant T fixed to match the damping profile of the experimental traces. As might be expected from the similarities in synthetic design and the TREPR spectra at 85K (Figure S1), and accounting the known differences in RP yield as determined from transient optical absorption measurements, the OOP-ESEEM data of **TTF-ANI-PI** and **TTF-ANI-PI$_2$** closely agree with each other and with the simulation.

TREPR spectra of TTF-ANI-PI and TTF-ANI-PI$_2$ at 200K

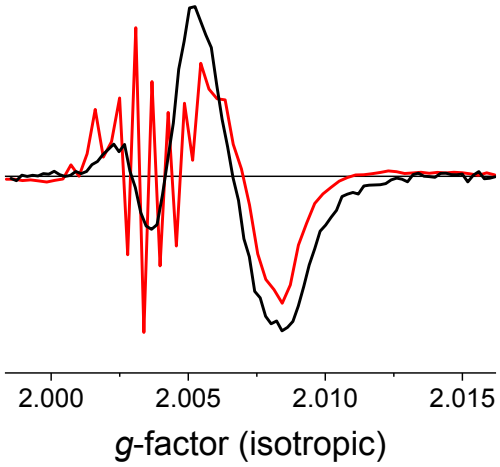

Figure S10. Normalized TREPR spectra of **TTF-ANI-PI** (red) and **TTF-ANI-PI$_2$** (black) at 200 ns after 416 nm laser flash at 200K in toluene-d_8.

Fitting of Transient ZQC in the Time Domain at Two Different Magnetic Field Points

The data points in Figure 7 in the main text can be fit to a function of the form:

$$F(T)_{3382G} = A_1 \sin(T\omega) e^{-T/t_l} + A_2[1 - \cos(T\omega)] e^{-T/t_l} \quad (4)$$

Where A is the amplitude, ω is the frequency of the oscillation, and t_l is the lifetime of the coherence.

$$F(T)_{3375G} = A_1 \sin(T\omega) e^{-T/t_l} + A_2[1 - \cos(T\omega)] e^{-T/t_l} + A_3 \sin(T\omega_2) e^{-T/t_l} + A_4[1 - \cos(T\omega_2)] e^{-T/t_l} \quad (5)$$

Using the same starting values for parameters of the same type between the two fits (e.g. amplitude, frequency, lifetime), the table below describes the results of the least-squares fit to the oscillations at each field point using the Levenberg-Marquardt algorithm.

Table S2. Fitting parameters of kinetic traces of ZQC in **TTF$^{+\bullet}$-ANI-PI$^{-\bullet}$** according to the above equations; observer fields and lifetimes of coherences are bolded for emphasis.

Field (mT)	A_1 (arb. unit)	A_2 (arb. unit)	ω (MHz)	A_3 (arb. unit)	A_4 (arb. unit)	ω_2 (MHz)	t_l (ns)
338.2	0.68	0.2224	24.4	N/A	N/A	N/A	**32.6**
337.5	0.07394	0.1424	30.02	-1.509	0.2704	8.322	**22.1**

References

1. Rees, A.; Sellergren, B.; Yilmaz, E.; Schrader, T., Affinity Material. Google Patents: 2013.

2. Gabutti, S.; Knutzen, M.; Neuburger, M.; Schull, G.; Berndt, R.; Mayor, M., A Rigid Sublimable Naphthalenediimide Cyclophane as Model Compound for Uhv Stm Experiments. *Chem. Commun.* **2008**, 2370-2372.

3. Schulten, K.; Wolynes, P. G., Semiclassical Description of Electron Spin Motion in Radicals Including the Effect of Electron Hopping. *J. Chem. Phys.* **1978**, *68*, 3292-3297.

4. Merkulov, I. A.; Efros, A. L.; Rosen, M., Electron Spin Relaxation by Nuclei in Semiconductor Quantum Dots. *Physical Review B* **2002**, *65*, 205309.

5. Weller, A.; Nolting, F.; Staerk, H., A Quantitative Interpretation of the Magnetic Field Effect on Hyperfine-Coupling-Induced Triplet Fromation from Radical Ion Pairs. *Chem. Phys. Lett.* **1983**, *96*, 24-27.

6. Tang, J.; Norris, J. R., Theoretical Calculations of Kinetics of the Radical Pair P_f State in Bacterial Photosynthesis. *Chem. Phys. Lett.* **1982**, *92*, 136-40.

7. Norris, J. R.; Morris, A. L.; Thurnauer, M. C.; Tang, J., A General Model of Electron Spin Polarization arising from the Interactions within Radical Pairs. *J. Chem. Phys.* **1990**, *92*, 4239-4249.

8. Tang, J.; Thurnauer, M. C.; Norris, J. R., Electron Spin Echo Envelope Modulation Due to Exchange and Dipolar Interactions in a Spin-Correlated Radical Pair. *Chem. Phys. Lett.* **1994**, *219*, 283-290.

9. Tang, J.; Norris, J. R., Multiple-Quantum EPR Coherence in a Spin-Correlated Radical Pair System. *Chem. Phys. Lett.* **1995**, *233*, 192-200.

10. Tang, J.; Thurnauer, M. C.; Norris, J. R., Abnormal Electron Spin Echo and Multiple-Quantum Coherence in a Spin-Correlated Radical Pair System. *Appl. Magn. Res.* **1995**, *9*, 23-31.

11. DiVincenzo, D. P., The Physical Implementation of Quantum Computation. *Fortschritte der Physik* **2000**, *48*, 771-783.

12. Carmieli, R.; Mi, Q.; Butler Ricks, A.; Giacobbe, E. M.; Mickley, S. M.; Wasielewski, M. R., Direct Measurement of Photoinduced Charge Separation Distances in Donor-Acceptor Systems for Artificial Photosynthesis Using OOP-ESEEM. *J. Am. Chem. Soc.* **2009**, *131*, 8372-8373.